[6] A. Homs-Corbera, D. Salvatella, J. A. Fiz, J. Morera, and R. Jané, "Time-frequency characterization of wheezes during forced exhalation," in *Abstr. 5h Conf. Eur. Soc. Eng. Med.*, Barcelona, Spain, 1999, pp. 423–424.
[7] A. Homs-Corbera, R. Jané, J. A. Fiz, and J. Morera, "Algorithm for time-frequency detection and analysis of wheezes," presented at the *22th Annu. Int. Conf. IEEE Engineering in Medicine and Biology Society World Congress 2000*, Chicago, IL, 2000.
[8] American Thoracic Society, "Standardization of spirometry," *Amer. Rev. Respir. Dis.*, vol. 136, pp. 1285–1298, 1987.
[9] J. Roca, J. Sanchis, and A. Agusti-Vidal *et al.*, "Spirometric reference from a Mediterranean population," *Bull. Eur. Physiopathol. Respir.*, vol. 22, pp. 217–224, 1986.
[10] H. Pasterkamp, S. S. Kraman, P. D. DeFrain, and G. R. Wodicka, "Measurement of respiratory acoustical signals. Comparison of sensors," *Chest*, vol. 104, pp. 1518–1525, 1993.

Real-Time Digital Signal Processing-Based Optical Coherence Tomography and Doppler Optical Coherence Tomography

Alexander W. Schaefer, J. Joshua Reynolds, Daniel L. Marks, and Stephen A. Boppart*

***Abstract*—We present the development and use of a real-time digital signal processing (DSP)-based optical coherence tomography (OCT) and Doppler OCT system. Images of microstructure and transient fluid-flow profiles are acquired using the DSP architecture for real-time processing of computationally intensive calculations. This acquisition system is readily configurable for a wide range of real-time signal processing and image processing applications in OCT.**

***Index Terms*—Digital signal processing, Doppler, optical coherence tomography (OCT), real-time imaging.**

I. Introduction

Optical coherence tomography (OCT) and Doppler OCT are emerging, high-resolution, biomedical imaging techniques. OCT is a real-time, noninvasive imaging technique that can achieve resolutions on the order of several microns [1]–[3]. Because OCT can acquire images that approach the resolution of histology, potential applications have been investigated in a wide range of medical and biological applications [4]–[7]. Doppler OCT has been developed in more recent years as a high-resolution method for detecting moving scatterers within a specimen, most commonly blood flow [8]–[15].

OCT generates images based on amplitude variations in the detected signal, whereas Doppler OCT generates images based on frequency (phase) variations. These techniques are analogous to ultrasound imaging and Doppler ultrasound, respectively, except reflections of near-infrared light are detected rather than sound. The shorter wavelengths of light compared to ultrasound give OCT and Doppler OCT nearly an order-of-magnitude improvement in imaging resolution. The theory and implementation of OCT and Doppler OCT have been thoroughly described in the literature [1]–[15]. In this paper, we describe the implementation and use of a novel digital-signal processing (DSP)-based acquisition system for OCT and Doppler OCT.

In the past, Doppler OCT was performed by acquiring data and processing it offline [8]–[11]. For example, blood flow rates were detected by computing a 32-point complex short-time Fourier transform for each pixel in a velocity image. The frequency centroid of the data was subtracted from the known frequency induced by a moving reference mirror to determine the Doppler shift. Computation of the 96 000 32-point complex short-time Fourier transforms for each image required 10 s to compute on a Pentium 200 [8]. To detect very slow velocities such as blood flow in capillaries, a phase-resolved Hilbert transform method has been used to achieve velocity sensitivities as high as 10 μm/s [12]. In this method, Doppler frequency shifts are detected by determining the instantaneous phase at each sampling point in the sample during an axial scan. A second axial scan is then acquired at the same position and the instantaneous phase is calculated again. The difference between each pair of instantaneous phase values at each sampling point along the axial scan, divided by the axial scan period, provides the instantaneous frequency induced by the scatterers. This technique assumes that a scatterer does not move far from the focal volume during the imaging process, and that it is not detected on a subsequent axial scan. Averaging phase differences between multiple axial scans improves the signal-to-noise ratio (SNR). To generate an image of 500 columns, a total of 4000 axial scans (eight per column) were acquired and processed. Therefore, image generation rate was on the order of one image every few seconds [12]. Recent advances in Doppler OCT have permitted the detection of higher fluid flow velocities up to approximately 1 m/s [11], [13], [15] and the use of an optical Hilbert transform [14] for high-sensitivity Doppler OCT imaging in real-time.

Real-time acquisition rates are a significant advantage in medical imaging. This advantage, however, is nullified when images are generated by first acquiring data and then postprocessed to extract information. To address this limitation and complement existing OCT and Doppler OCT techniques, we have designed and implemented a real-time DSP-based OCT and Doppler OCT acquisition system that uses a preprocessing field-programmable gate array (FPGA) and a programmable DSP to manage computationally intense algorithms in real time. This system is used to measure fluid flow transients in a capillary tube. The current system supports both structural and velocity-based images (500 $\times$ 500 pixels) that can be acquired at 8 frames/s (fps). This flexible DSP-based system can easily be modified to support other signal processing techniques such as spectroscopic OCT [16] or digital dispersion compensation [17], taking full advantage of the high-speed acquisition rates of OCT.

II. Materials and Methods

An FPGA and a programmable DSP were integrated between the analog detection electronics and the host personal computer (PC) of an existing OCT system to enable real-time signal and image processing. As a result, the image generation and data acquisition rates were equivalent.

Manuscript received May 7, 2002; revised April 18, 2003. This work was supported in part by the National Science Foundation (NSF) under Grant BES-0086696, in part by the Whitaker Foundation, and in part by the Beckman Institute. *Asterisk indicates corresponding author.*

A. W. Schaefer, J. J. Reynolds, and D. L. Marks are with the Department of Electrical and Computer Engineering, Beckman Institute for Advanced Science and Technology, University of Illinois at Urbana-Champaign, Urbana, IL 61801 USA.

*S. A. Boppart is with the Department of Electrical and Computer Engineering, Bioengineering Program, Beckman Institute for Advanced Science and Technology, College of Medicine, University of Illinois at Urbana-Champaign, 405 N. Mathews Avenue, Urbana, IL 61801 USA (e-mail: boppart@uiuc.edu; website: http://nb.beckman.uiuc.edu/biophotonics).

Digital Object Identifier 10.1109/TBME.2003.820369

A. Rapid-Scanning Optical Delay Line

To perform real-time OCT and Doppler OCT data acquisition, a high-speed grating-based phase delay line was implemented [18]. This delay line is based on the principles of femtosecond pulse shaping [19]. The optical delay line is responsible for setting the center frequency of the interference waveform. A resonant scanner in the delay line was driven by a sinusoidal waveform with a frequency of 4 kHz. The frequency induced by our delay line could be set to a value from 2 to 4 MHz. Because the resonant scanner produces a sinusoidal variation in the optical delay, data was acquired with a 16% duty cycle, during the approximately linear region of the sinusoid. The frequency variation in this linear region was measured to be within 5%. Although the optical delay line allows for data acquisition at a rate of 8000 columns/s, data was acquired at a slower rate due to limitations in the PCI bus transfer rate.

B. Digital Signal Processing Hardware

Digital signal processing was performed on a sampled interference waveform. The optical signal was first detected, amplified, and filtered in the analog domain. A photodiode converted the optical interference waveform into an electrical current. The output voltage from a high-gain, wideband, unity-gain stable, finite—element transfer input transimpedance amplifier was ac-coupled to a second amplification stage with variable gain. A fourth-order Butterworth bandpass filter (BPF) with a passband from 1 MHz to 6 MHz followed the gain stage and supported a wide range of Doppler-shifted frequencies.

In the FPGA architecture (Heron I/O 2 module, Traquair Data Systems, Inc.), a 12-bit analog-to-digital converter sampled the output of an analog unity gain buffer at 25 MS/s. A digital BPF further increased the SNR by filtering noise outside of a passband that was narrower than the analog BPF. To determine frequency shifts in the detected signal that corresponded to moving scatterers, an amplitude-independent frequency demodulation scheme was implemented with the Hilbert transform to compute both the instantaneous phase and amplitude of the signal [20]. The variation in instantaneous phase and amplitude along an axial scan was used to generate Doppler OCT and structural OCT images, respectively. The instantaneous frequency was determined by taking the difference between two consecutive phases and dividing by the sampling period.

The output of the digital BPF was sent to the Hilbert filter and subsequently, the in-phase and quadrature outputs of the Hilbert filter were forwarded to the DSP where both the instantaneous frequency and magnitude of each Hilbert filter output were computed. The PC read the amplitude and velocity data one column at a time, corresponding to one axial scan, and aligned adjacent columns for image display. Images 500 $\times$ 500 pixels in size were acquired at 8 fps. Higher frame rates were limited by the sustained 4 Mbytes/s PCI bus transfer rates of the PC.

The FPGA architecture can be divided into three main sections: a data processing block, a waveform generation block, and a control block. The majority of the logic resources were dedicated to the processing block, which consisted of two finite impulse response (FIR) filters implemented using a distributed arithmetic FIR filter core. Both filters were designed using MATLAB (Natick, MA). The filter characteristics of the digital BPF were programmable and configured based on the center frequency (e.g., 3 MHz) and bandwidth (e.g., 2 MHz) of the expected signal. Both the BPF and the Hilbert filter achieved a signal-to-quantization noise ratio of over 60 dB. The filters were realized using logic cores (Xilinx Core Generator 3.1) [21].

The waveform generation block consisted of a register and accumulator to generate the x axis galvanometer waveform to scan the imaging beam and a read-only memory to generate the sinusoid to drive the resonant scanner in the optical delay line (z axis). The control block coordinated the activities of the processing and waveform generation blocks and managed communication with the DSP. Following a user reset, control values read from the DSP allowed for changing the image size, location, and the sweep of the x axis galvanometer. A 32 wide $\times$ 512 deep first-in-first-out data buffer was also implemented to buffer the filtered data prior to being read by the programmable DSP, allowing for higher priority assignments to both computations and forwarding image data to the PC. The FPGA design occupied approximately two-thirds of the available logic slices. The system clock rate of the FPGA was 50 MHz and the sampling rate was set to 25 MS/s.

A programmable DSP (C6701 processor, Texas Instruments Inc.) operating at 132 MHz was implemented in this system. The output of the Hilbert filter was further processed to obtain both the instantaneous magnitude and frequency of each output sample. The most computationally intense operation performed was the approximation of $\arctan(Im/Re)$ for each Hilbert filter output. A C-callable assembly routine was written to compute both the instantaneous phase and magnitude for each in-phase and quadrature output of the Hilbert filter obtained in an axial scan. A look-up table in the data cache stored values of $\arctan(Im/Re)$ over a range of 0° to 45° and symmetry extended this range to 360°. The center frequency of the optical delay line was subtracted from the instantaneous frequency values to determine Doppler shifts induced by scatterers. Positive and negative frequency shifts could be observed.

The maximum detectable velocity varied with the bandwidth of the digital BPF as well as the angle between the incident beam and the direction of fluid flow. For a 2-MHz bandwidth and a 45° incident angle, bidirectional flow rates of up to $\pm$50 cm/s could be detected. The minimum detectable velocity was approximately 3% of the detected frequency range, determined by the root-mean-square (RMS) error from an ideal constant-frequency input waveform. More sensitive velocity detection could be achieved by reducing the detected velocity range.

C. OCT/Doppler OCT System Specifications

The optical system in this study included a solid-state ($\mathrm{Nd:YVO_4}$) diode-pumped titanium:sapphire ($\mathrm{Ti:Al_2O_3}$) laser operating at 800 nm center wavelength and a spectral bandwidth of approximately 30 nm. The axial resolution and transverse resolutions of the system were 10 μm and 15 μm, respectively. The dynamic range of the OCT system was greater than 100 dB as determined by the ratio of the signal amplitude at the output of the detection electronics when imaging a mirror (perfect reflector) compared to when the sample arm is blocked (noise floor). The optical power delivered to the sample was 50 mW. The experimental setup is shown in Fig. 1(a). The angle between the incident beam and the glass tube was 70°.

For the images presented here, overlap in the gray-scale maps was used to enhance the contrast between flow rates at different areas in the tube. For regions in the sample that had minimal optical backscatter, only noise fell within the passband of the digital BPF. Therefore, the instantaneous velocities at these locations were random. Rather than display the random data, Hilbert filter output samples with instantaneous amplitudes lower than a specified threshold were assumed to be noise and were not displayed. The pixel values at these locations were set to zero (black) in the images.

III. Results

A. DSP-Based OCT and Doppler OCT

To demonstrate the performance of our DSP-based acquisition system, real-time Doppler OCT images of fluid-flow profiles in a glass capillary tube were acquired. Fig. 1(b)-(c) shows a photograph and OCT image of the tube, respectively. A glass cylindrical extrusion

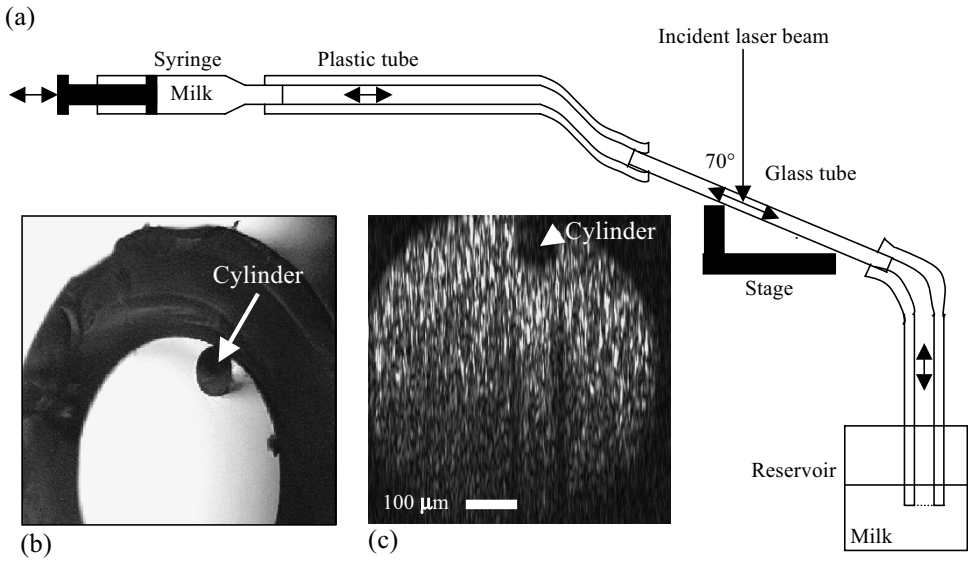

Fig. 1. Experimental setup. (a) Fluid delivery and imaging system consisted of a syringe pump, plastic and glass tubes, and a fluid reservoir. The OCT beam is scanned across the glass capillary tube. (b) Light microscopy image of the cross section of the capillary tube. (c) Structural OCT image of the capillary tube with stationary fluid. Note the presence of the internal cylinder defect in (b) and (c) which spans the entire length of the tube.

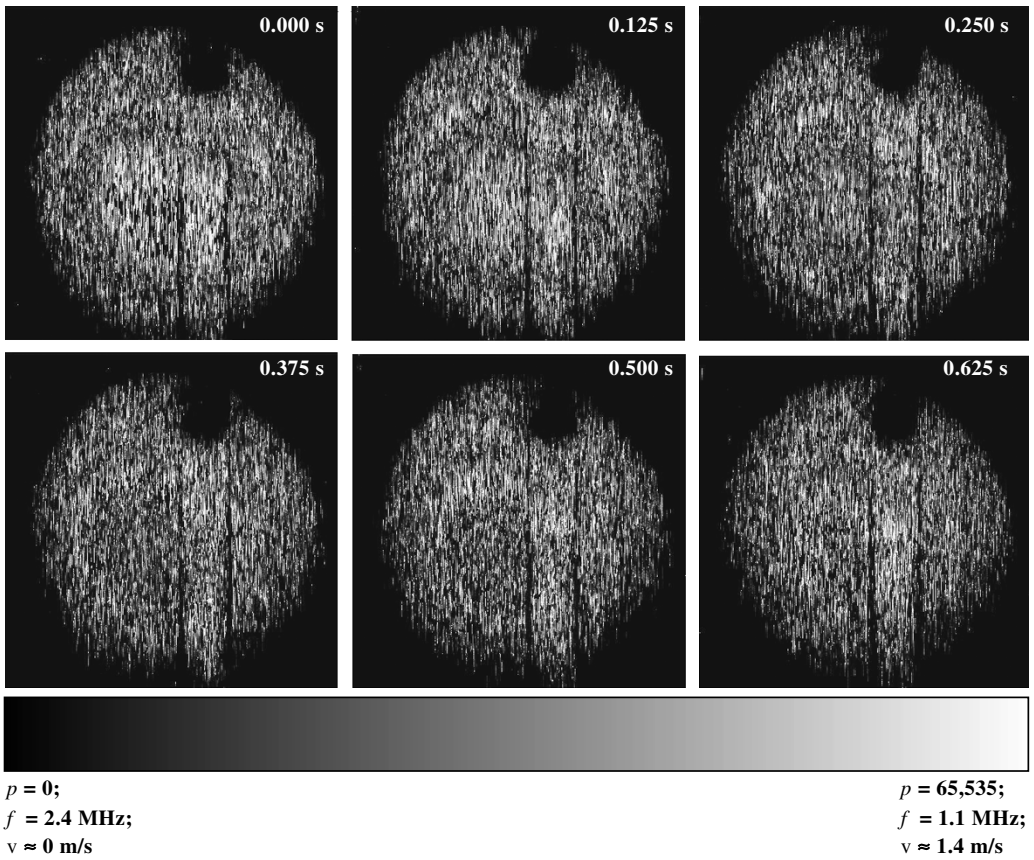

Fig. 2. Real-time Doppler OCT of fluid flow. A sequence of six images was acquired during a fluid flow transient caused by turning off the syringe pump. Two sets of rings can be observed in the first image. The rings collapse during the reduction in fluid flow velocity. The time is indicated in each image. The gray-scale bar indicates the pixel values (p), the instantaneous frequency (f), and the fluid flow velocity (v), corresponding to the respective intensity in the images.

defect within the capillary tube is observed. Diluted (10%) milk was used as a liquid with scattering particles (lipids and proteins). Note the reduced backscatter intensity toward the bottom of the tube [Fig. 1(c)] due predominantly to the scattering of the milk.

Fig. 2 shows a series of six images taken during a 625-ms transient that took place when the syringe pump was turned off and flow velocity was decreasing. The approximate gray-scale of the velocity-based images is shown. Note the presence of rings that form around the center of the channel and the cylinder along the inner diameter of the tube. The center of the image changes in both intensity and diameter during the first four images. The outer rings indicate an intermediate flow velocity that begins to diminish in the last few images.

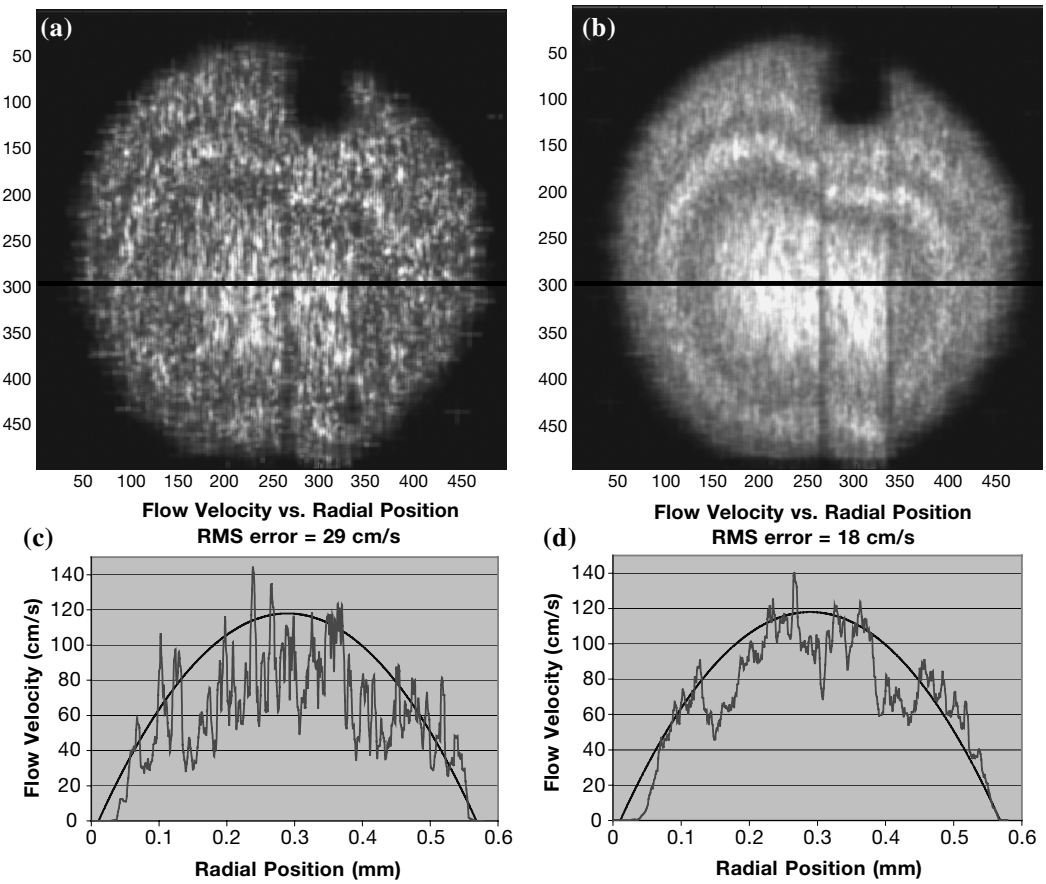

Fig. 3. Image processing. (a) Neighborhood averaged velocity image. (b) Average of eight processed images acquired during a constant fluid flow. (c) Cross-sectional profile taken along the horizontal line in (a) with a superimposed theoretical flow profile. (d) Cross-sectional profile taken along the horizontal line in (b) with a superimposed theoretical flow profile.

B. Postacquisition Image Processing

The flow-rate images allow one to qualitatively observe a fluid-flow transient. These raw images are displayed without additional image processing. Additional image processing steps that can be performed in real-time with additional DSP hardware components are presented. To improve the image quality and characterization accuracy of the system, three image processing steps were performed: interpolation, neighborhood averaging, and image averaging. The first step involved interpolation to assign values to zeroed pixels that did not meet the minimum amplitude threshold. A 5×5 neighborhood-averaging algorithm was employed. Fig. 3(a) shows a processed image of the flow in the tube with an average volumetric flow rate of 10 mL/min. A cross-sectional profile taken along the horizontal line is shown in Fig. 3(c) along with the theoretical flow profile. There has been a considerable reduction in variation along the cross section. The RMS difference between the two plots is 29 cm/s, which is less than 25% of the theoretical maximum velocity.

The third processing step involves averaging several images associated with a constant flow rate. Fig. 3(b) shows an image obtained by averaging eight interpolated, neighborhood-averaged images. Each image was acquired during a constant volumetric flow rate. A cross section taken along the horizontal line is shown in Fig. 3(d) along with the theoretical flow profile. The RMS difference between these two plots is 18 cm/s, which is less than 15% of the theoretical maximum velocity.

IV. Discussion

We have demonstrated the use of FPGA and DSP hardware to perform real-time OCT and Doppler OCT. Images 500×500 pixels in size have been generated at 8 fps allowing for observation of fluid flow transients in real-time. To further improve visualization of fluid-flow profiles, additional processing steps can be performed in real time with additional DSP hardware. The DSP hardware implemented with this system is readily configurable, allowing for the implementation of future high-speed signal processing and image processing algorithms.

There are spatially localized variations in the data obtained for the fluid-flow rate images shown in Fig. 2. These variations affect image quality, which is dependent on a number of factors. The center frequency from the optical delay line varies with distance along an axial scan. This sinusoidal frequency variation is directly proportional to the resonant scanner's angular position with time. By acquiring data along the most linear region of the sinusoid, the effects of this variation can be reduced. In our system, the frequency variation was less than 5%.

The incident beam is subject to scattering, absorption, and dispersion as it penetrates into the sample. Scattering particles often reflect light away from the interferometer and are not detected. Due to the low signal amplitude obtained, these locations were set to zero resulting in numerous black pixels in the images. Therefore, a cross section of the flow rate image does not result in a noise-free, parabolic flow profile. Three image processing steps were performed to improve the quality of the images. A second DSP board (TI C6701) could perform these image processing steps in real time.

The capabilities of this digital acquisition and processing system will enable a wide range of investigational studies of fluid-flow transients in dynamic microfluidic devices as well as in living microfluidic systems such as the human microcirculatory system and developmental biology animal models. The use of combined FPGA-DSP hardware

will enable future implementations of fully configurable, all-digital acquisition systems, eliminating most of the analog electronics present in OCT systems. This technology expands the high-speed, real-time diagnostic capabilities of OCT and Doppler OCT and will enable complex OCT-based signal and imaging processing to be performed in real time.

ACKNOWLEDGMENT

The authors would like to acknowledge the technical assistance of Dr. A. Oldenburg and J. Reynolds for maintaining and operating the OCT system. They would also like to thank S. Chappell for her assistance in editing and assembling this manuscript.

REFERENCES

[1] D. Huang, E. A. Swanson, C. P. Lin, J. S. Schuman, W. G. Stinson, W. Chang, M. R. Hee, T. Flotte, K. Gregory, C. A. Puliafito, and J. G. Fujimoto, "Optical coherence tomography," *Science*, vol. 254, pp. 1178–1181, 1991.

[2] B. E. Bouma and G. J. Tearney, Eds., *Handbook of Optical Coherence Tomography*. New York: Marcel Dekker, 2001.

[3] J. M. Schmitt, "Optical coherence tomography (OCT): A review," *IEEE J. Select. Topics Quantum Electron.*, vol. 5, pp. 1205–1215, July-Aug. 1999.

[4] J. G. Fujimoto, C. Pitris, S. A. Boppart, and M. E. Brezinski, "Optical coherence tomography: An emerging technology for biomedical imaging and optical biopsy," *Neoplasia*, vol. 2, pp. 9–25, 2000.

[5] G. J. Tearney, M. E. Brezinski, B. E. Bouma, S. A. Boppart, C. Pitris, J. F. Southern, and J. G. Fujimoto, "*In vivo* endoscopic optical biopsy with optical coherence tomography," *Science*, vol. 276, pp. 2037–2039, 1997.

[6] A. Das, M. V. Sivak Jr., A. Chak, R. C. Wong, V. Westphal, A. M. Rollins, J. Willis, G. Isenberg, and J. A. Izatt, "High-resolution endoscopic imaging of the GI tract: A comparative study of optical coherence tomography versus high-frequency catheter probe EUS," *Gastrointest. Endosc.*, vol. 54, pp. 219–224, 2001.

[7] S. A. Boppart, B. E. Bouma, C. Pitris, J. F. Southern, M. E. Brezinski, and J. G. Fujimoto, "*In vivo* cellular optical coherence tomography imaging," *Nature Med.*, vol. 4, pp. 861–864, 1998.

[8] J. A. Izatt, M. D. Kulkarni, S. Yazdanfar, J. K. Barton, and A. J. Welch, "*In vivo* bidirectional color Doppler flow imaging of picoliter blood volumes using optical coherence tomography," *Opt. Lett.*, vol. 22, pp. 1439–1441, 1997.

[9] S. Yazdanfar, M. D. Kulkarni, and J. A. Izatt, "High-resolution imaging of *in vivo* cardiac dynamics using color Doppler optical coherence tomography," *Opt. Express*, vol. 1, pp. 424–431, 1997.

[10] Z. Chen, Y. Zhao, S. M. Srinivas, J. S. Nelson, N. Prakash, and R. D. Frostig, "Optical Doppler tomography," *IEEE J. Select. Topics Quantum Electron.*, vol. 5, pp. 1134–1142, 1999.

[11] T. G. van Leeuwen, M. D. Kulkarni, S. Yazdanfar, A. M. Rollins, and J. A. Izatt, "High-flow-velocity and shear-rate imaging by use of color Doppler optical coherence tomography," *Opt. Lett.*, vol. 24, pp. 1584–1586, 1999.

[12] Y. Zhao, Z. Chen, C. Saxer, S. Xiang, J. F. de Boer, and J. S. Nelson, "Phase-resolved optical coherence tomography and optical Doppler tomography for imaging blood flow in human skin with fast scanning speed and high velocity sensitivity," *Opt. Lett.*, vol. 25, pp. 114–116, 2000.

[13] V. Westphal, S. Yazdanfar, A. M. Rollins, and J. A. Izatt, "Real-time, high velocity-resolution color Doppler optical coherence tomography," *Opt. Lett.*, vol. 27, pp. 34–36, 2002.

[14] Y. Zhao, Z. Chen, Z. Ding, H. Ren, and J. S. Nelson, "Real-time phase-resolved functional optical coherence tomography by use of optical Hilbert transformation," *Opt. Lett.*, vol. 27, pp. 98–100, 2002.

[15] A. M. Rollins, S. Yazdanfar, J. K. Barton, and J. A. Izatt, "Real-time *in vivo* color Doppler optical coherence tomography," *J. Biomed. Opt.*, vol. 7, pp. 123–129, 2002.

[16] U. Morgner, W. Drexler, F. X. Kartner, X. D. Li, C. Pitris, E. P. Ippen, and J. G. Fujimoto, "Spectroscopic optical coherence tomography," *Opt. Lett.*, vol. 25, pp. 111–113, 2000.

[17] D. L. Marks, A. L. Oldenburg, J. J. Reynolds, and S. A. Boppart, "Digital algorithm for dispersion correction in optical coherence tomography for homogeneous and stratified media," *Appl. Opt.*, vol. 42, pp. 204–217, 2003.

[18] G. J. Tearney, B. E. Bouma, and J. G. Fujimoto, "High-speed phase- and group-delay scanning with a grating-based phase control line," *Opt. Lett.*, vol. 22, pp. 1811–1812, 1997.

[19] A. M. Weiner, "Femtosecond pulse shaping using spatial light modulators," *Rev. Scientific Instrum.*, vol. 71, pp. 1929–1960, 2000.

[20] J. N. Pandey, *The Hilbert Transform of Schwartz Distributions and Applications*. New York: Wiley, 1995.

[21] Xilinx Inc.. (2001) Xilinx Core Generator System. [Online]. Available: http://www.xilinx.com/products/logicore/coregen/index.htm

Signal Processing Methodology to Study the Cutaneous Vasodilator Response to a Local External Pressure Application Detected by Laser Doppler Flowmetry

Anne Humeau*, Lionel Fizanne, Ambroise Garry, Jean-Louis Saumet, and Jean-Pierre L'Huillier

***Abstract*—The existence of a cutaneous pressure-induced vasodilation (PIV) has recently been reported. This paper proposes a signal processing methodology to improve PIV knowledge. Temporal variations of laser Doppler signals rhythmic activities are first analyzed on anesthetized rats. The results lead to a method that provides a better PIV understanding.**

***Index Terms*—Laser Doppler, microcirculation, pressure, rat, scalogram.**

I. INTRODUCTION

Laser Doppler flowmetry (LDF) is a noninvasive method to monitor skin perfusion. Several signal processing studies have been carried out on human LDF recordings. These analyses demonstrated the existence of five characteristic frequency peaks on the time scale of around 1 min [1]–[3]. The LDF technique has also recently been used to report a significant transient increase of the cutaneous blood flow signal during a local nonnoxious pressure applied progressively in the skin [4]. This local pressure-induced vasodilation (PIV) exists in rats, as in humans. However, PIV is still not entirely understood even if some results have helped in the understanding of this phenomenon [4]–[7]. It is proposed that this response is a protective mechanism without which certain pressure-associated lesions may develop. The existence of this vasodilatory reflex response to nonnoxious pressure strain may also have important implications for the cutaneous pathologies involved in various neurological diseases and in the pathophysiology of decubitus ulcers [8].

In order to have a better understanding on the mechanisms generating this phenomenon, a deep analysis on PIV signals has now become highly important. This paper, therefore, proposes a first *methodology of work* to initiate a complete signal processing study in this field.

Manuscript received November 28, 2002; revised May 1, 2003. *Asterisk indicates corresponding author.*

*A. Humeau is with the Groupe ISAIP-ESAIP, 18 rue du 8 mai 1945, BP 80022, 49180 Saint Barthélémy d'Anjou Cedex, France (e-mail: ahumeau@isaip.uco.fr).

L. Fizanne, A. Garry, and J.-L. Saumet are with the Laboratoire de Physiologie, Faculté de Médecine, 49045 Angers Cedex, France.

J.-P. L'Huillier is with the Laboratoire Procédés—Matériaux—Instrumentation (L.P.M.I.), Ecole Nationale Supérieure d'Arts et Métiers (E.N.S.A.M.), 49035 Angers Cedex, France.

Digital Object Identifier 10.1109/TBME.2003.820371